

Interfacial Engineering Designed on CuSCN for Highly Efficient and Stable Carbon-based Perovskite Solar Cells

Fanning Meng¹, Ligu Gao^{1,*}, Anmin Liu¹, Yanqiang Li¹, and Tingli Ma^{2,3,*}

¹ State Key Laboratory of Fine Chemicals, School of Chemical Engineering, Dalian University of Technology, Dalian, 116023, P. R. China

² Department of Materials Science and Engineering, China Jiliang University, Hangzhou, 310018, P. R. China

³ Graduate School of Life Science and Systems Engineering, Kyushu Institute of Technology, Kitakyushu, Fukuoka 808-0196, Japan

Corresponding Authors

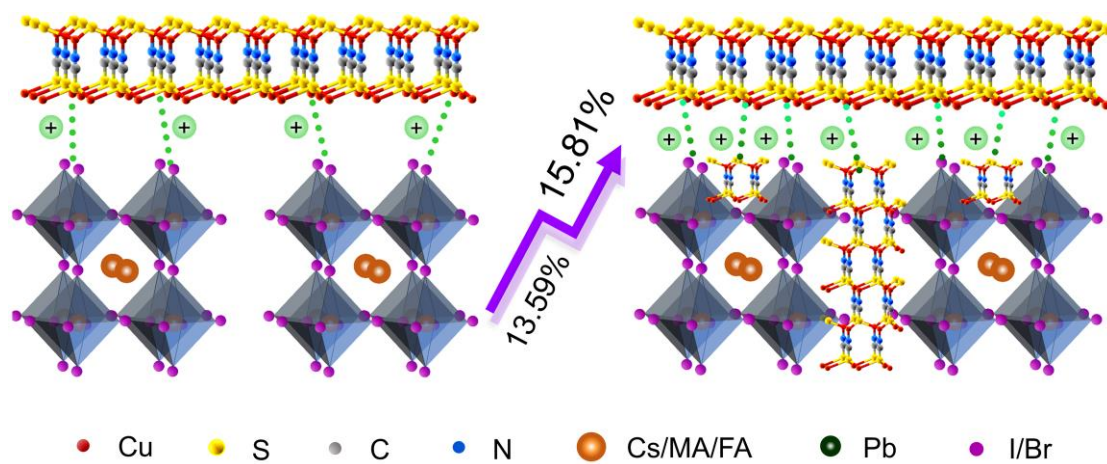
*Ligu Gao

Tel: +86-427-2631810. E-mail: liguo.gao@dlut.edu.cn; ORCID: 0000-0002-5390-3663.

*Tingli Ma

Tel: 093-695-6045. E-mail: tinglima@life.kyutech.ac.jp; ORCID: 0000-0002-3310-459X.

Graphical abstract



Abstract

The undesired energy level alignment and charge recombination at the perovskite/carbon electrode interface limit the application of carbon-based perovskite solar cells (C-PSCs). The incorporation of hole transport materials, CuSCN, is an effective strategy to solve this issue. However, the mismatched crystal structure and lattice between perovskite layer (cubic crystal) and CuSCN layer (hexagonal crystal) lead to charge transport barrier due to the gaps at the heterogeneous interface. Herein, the interfacial engineering designed on CuSCN has been carried out, which not only improves the quality of perovskite film but also reduces the defects, enhances the interfacial connection, and ensures rapid charge extraction and transfer. After key parameter adjustment, both high efficiency (15.81%) and good stability of C-PSCs have been obtained. After storage for 2000 h at ambient air environment, devices without any encapsulation could maintain 93% of its initial efficiency. The thermal stability test shows that the encapsulated devices retain 83% of its initial efficiency after storage for 300 h in a dry air at 85 °C. The deep insight and mechanism have been proposed in this interfacial engineering design for improving the efficiency and stability of C-PSCs.

Key words: Perovskite solar cells, CuSCN, Interfacial engineering, Inorganic hole transport material

Introduction

In about a decade, the research on perovskite solar cells (PSCs) have drawn extensive attention due to the prominent optical and electrical properties of perovskite (PVK) materials such as large absorption coefficient, high carrier mobility, and tunable bandgap [1-4]. To date, the certified power conversion efficiency (PCE) has reached 25.5% [5]. However, two main issues obstacle the commercialization of PSCs: the device instability and high cost [6-10]. Benefiting from low cost, abundant source and strong hydrophobicity of carbon materials, carbon-based PSCs (C-PSCs) could reduce the cost of devices, save the energy consumption of fabrication process and significantly improve the device stability (over 10,000 h stability) [11, 12]. However, C-PSCs suffer lower PCE because of the undesirable energy level alignment and serious charge recombination at the PVK/carbon electrode interface [13-15], where the organic hole transport materials (HTMs) could not be applied due to their chemical and thermal instability [16-18]. Therefore, much more thermally and chemically stable inorganic HTMs are used in C-PSCs, including CuSCN [19], NiO_x [20], CuI [21], CuPc [22], Cu_xS [23], etc. Among various inorganic HTMs, CuSCN is an extremely cheap, abundant p-type semiconductor with high hole mobility, good thermal stability, and a well-aligned work function [24]. In 2018, Mashhoun et al. showed that CuSCN could work more efficiently than poly(3-hexylthiophene-2,5-diyl) as HTMs in C-PSCs [25]. Subsequently, Wu et al. constructed CuSCN/carbon nanotubes back contact to guarantee effective hole extraction and collection for C-PSCs, obtaining high PCE and good stability simultaneously [26]. Arora et al. designed a robust and highly efficient architecture on the basis of CuSCN, ascertaining long-term operational stability and ultraviolet illumination stability without compromising efficiency [27]. Yang et al. deeply revealed the underlying dynamic process of generation, separation, extraction, and transfer of hole carriers at the PVK/CuSCN (or Spiro-OMeTAD) interface [28]. Zimmermann et al. addressed the problem of unbalanced charge extraction in mesoscopic HTM-free C-PSCs

through constructing a bulk heterojunction between PVK and CuSCN [29]. Although many studies on CuSCN have been carried out, the fact that CuSCN used as HTMs has a hexagonal crystal structure is always ignored [30], which does not match with a cubic crystal structure of the PVK layer. Therefore, many gaps will generate at the heterogeneous interface between the PVK layer and the CuSCN layer due to the mismatched structure and lattice, resulting in charge transport barrier and serious recombination.

To deal with this issue, interfacial engineering designed on CuSCN is carried out in this work via a two-step procedure, accompanying crystal growth and serving as HTMs. The accompanying crystal growth is implemented by the modified antisolvent procedure. Comparing with the pristine antisolvent procedure, the modified antisolvent procedure plays an important role in the nucleation, crystal growth, and film formation of PVK [31-34]. Through the CuSCN modified antisolvent treatment, the quality of the PVK film is improved, the defects of the grains are passivated, and the density of trap states is reduced. Subsequently, CuSCN is dynamically spin-coated on the surface of the passivated PVK and served as a hole transport layer. Results demonstrate that the reduced trap states and enhanced connection are achieved at the heterogeneous interface between the passivated PVK layer and the CuSCN layer, leading to high PCE (15.81%) and good stability of CuSCN-based C-PSCs. The devices without any encapsulation maintain 93% of the initial efficiency after storage for 2000 h at ambient air.

Results and discussion

The pristine PVK film was prepared by pure chlorobenzene in a typical antisolvent process. The passivated PVK film was fabricated by a modified antisolvent procedure, where CuSCN was introduced into the chlorobenzene antisolvent. The detail experiments are described in the Supporting Information. Although CuSCN is insoluble in chlorobenzene, colloidal solution of CuSCN without any precipitate could be obtained by magnetic stirring and ultrasonic dispersion. This

colloidal solution was used to perform the modified antisolvent procedure. Due to the Lewis base properties of SCN^- , CuSCN could possibly passivate the defects of PVK crystals, retard the crystallization process and generate large PVK grains. X-ray diffraction (XRD) analysis was conducted to investigate the crystallinity of the PVK film. In Figure 1a, the clear diffraction peaks at 14.1° , 28.4° , and 31.8° can be indexed to the (110), (220) and (310) reflection of PVK crystal structure. In comparison with the pristine PVK, the full-width-half-maxima of (110), (220) and (310) crystal planes for the passivated PVK is slightly decreased, as shown in Table S1. It indicates that the passivated PVK has an improved crystallinity. Meanwhile, almost no shift of the main characteristic XRD peaks is observed in the passivated PVK, suggesting that the CuSCN does not participate in constructing the PVK framework [35].

To determine the distribution of CuSCN particles, energy dispersive X-ray spectroscopy (EDS) analysis of the S and Cu elements was carried out. The EDS elemental mapping in Figure S1 shows that CuSCN particles cover the whole surface of the passivated PVK film. Further, atomic force microscopy (AFM) images of the pristine PVK film, the passivated PVK film, and the CuSCN film are characterized, as shown in Figure 1b, c and Figure S2. The AFM results indicate that the particulate CuSCN is located around the grain boundaries of the passivated PVK film. Given the fact that the crystal lattice and parameters between CuSCN and PVK are different, the location of CuSCN was also identified through High Resolution Transmission Electron Microscope (HRTEM). As shown in Figure S3, the different lattice fringes of CuSCN are observed at the boundary of PVK grains, demonstrating its presence at the grain boundaries. Meanwhile, depth profile information is necessary to obtain CuSCN distribution. As shown in Figure 1d, e and Figure S4, the particulate CuSCN is partially embedded into the passivated PVK film. According to the AFM, TEM and EDS results, the particulate CuSCN is homogeneously distributed on the surface and inside of the passivated PVK film, which makes it possible to establish the PVK-CuSCN bulk heterojunction.

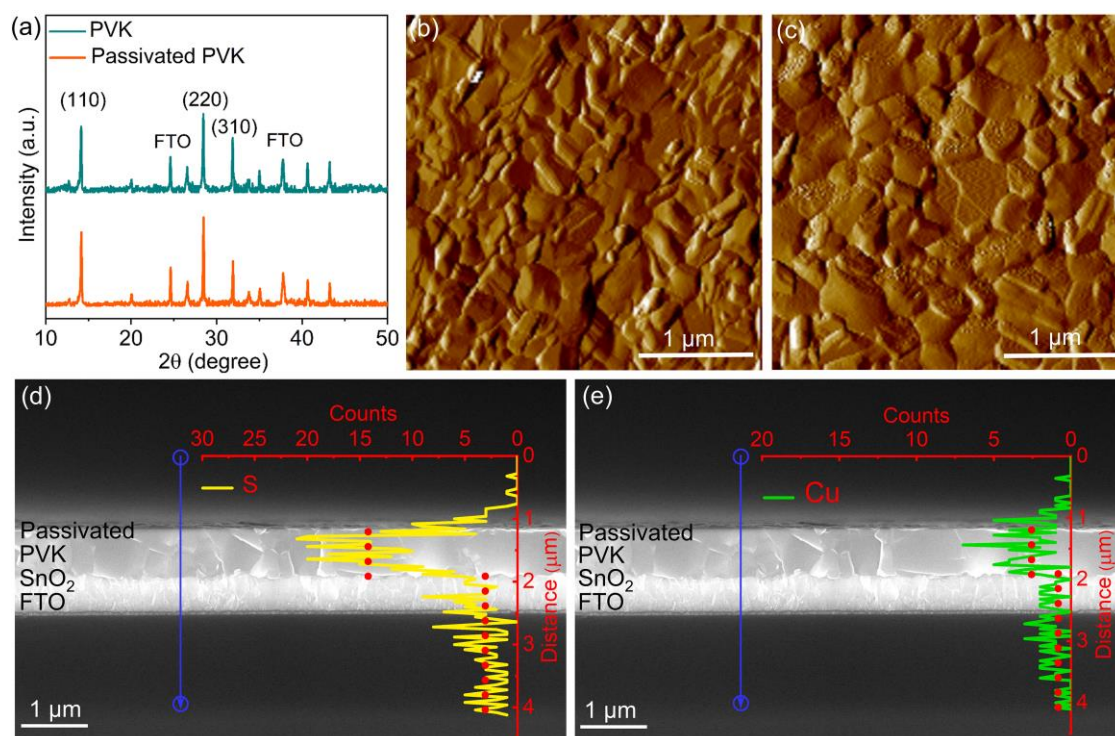


Figure 1. (a) XRD patterns of the pristine PVK and the passivated PVK films on the FTO substrates, (b) the AFM image of the pristine PVK film, (c) the AFM image of the passivated PVK film, (d) the S element and (e) the Cu element profiles across the FTO/SnO₂/passivated PVK sample determined by EDS line scan.

To ascertain the influence of CuSCN in antisolvent on PVK morphology, scanning electron microscope (SEM) measurements were performed. As shown in Figure 2a and b, larger grains can be obtained in the passivated PVK film rather than the pristine one, which indicates that the CuSCN plays a positive role in facilitating crystal growth. We speculate that the interaction of Pb²⁺ and SCN⁻ could suppress the nucleation and decrease the growth rate of the PVK grains, leading to larger grains [36-38]. The larger grains result in the enhanced visible light absorption (Figure S5). Moreover, AFM results in Figure 2c and d indicate that the root mean square roughness decreases from 27.4 nm (the pristine PVK film) to 21.5 nm (the passivated PVK film) due to the CuSCN passivation. The smoother surface morphology of the passivated PVK film is favorable to enhance the interfacial connection with the post-deposited hole transport layer [39].

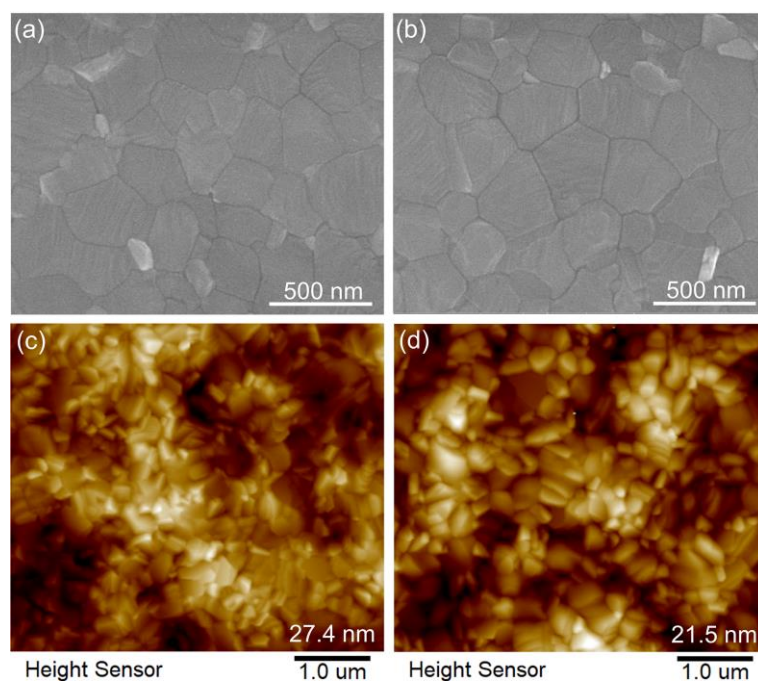


Figure 2. SEM images of (a) the pristine PVK film and (b) the passivated PVK film, AFM images of (c) the pristine PVK film and (d) the passivated PVK film.

X-ray photoelectron spectroscopy (XPS) was further conducted to deeply investigate the crystallite quality of the PVK film, as shown in Figure 3a. The Pb 4f spectra exhibit two main peaks, Pb 4f_{5/2} at 143.3 eV and Pb 4f_{7/2} at 138.4 eV, respectively. And there are two small satellite peaks at around 141.6 eV and 136.6 eV, which assign to undercoordinated Pb²⁺ in the mixed-cation PVK film. The undercoordinated Pb²⁺ species in the PVK film act as trap states, which could lead to unfavorable non-radiative recombination and impair solar cell performance [40]. In comparison with the pristine PVK film, satellite peaks of the passivated PVK film are substantially weakened, indicating its lower trap states. Meanwhile, the peaks of Pb 4f_{5/2} and Pb 4f_{7/2} in the passivated PVK film shift towards lower binding energy in comparison with those of the pristine PVK film (Figure S6), which implies the increase of electron cloud density around Pb²⁺ under the influence of SCN⁻. Fourier transform infrared spectroscopy (FTIR) in Figure S7 also confirms the same result. The C–S band shifts from 877 cm⁻¹ for CuSCN to 862 cm⁻¹ for the passivated PVK, implying the bonding interaction between Pb²⁺ and SCN⁻. Therefore, SCN⁻ with lone

pairs of electrons acts as a Lewis base and interacts with undercoordinated Pb^{2+} ions, resulting in the lower trap states of the passivated PVK. In addition, the interaction between Pb^{2+} and SCN^- can provide an anchor effect for the adhesion of CuSCN nanoparticles on PVK grains with large surface area. This could ensure good contact between CuSCN nanoparticles and PVK grains.

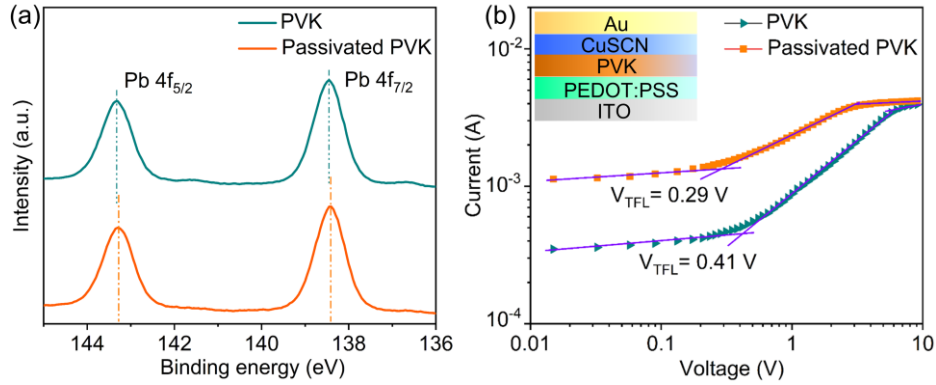


Figure 3. (a) XPS spectra of the pristine PVK and the passivated PVK films, (b) dark current–voltage curves of hole-only devices based on the pristine PVK and the passivated PVK films, the inset displays the structure of hole-only devices.

To quantitatively calculate the trap state density of both pristine PVK and passivated PVK films, the space-charge-limited current (SCLC) model was utilized. The dark current–voltage characteristics of the hole-only devices are shown in Figure 3b. At a low bias voltage, the current signal increases linearly as the voltage, corresponding to the ohmic regime. And then the current displays dramatically nonlinear rising at a middle bias voltage, corresponding to the trap-filled limited (TFL) regime. Eventually, the current exhibits quadratic voltage dependence at a high bias voltage, corresponding to the trap-free SCLC regime. The trap state density can be estimated from the trap-filled limit voltage (V_{TFL}) via the following Equation [41]:

$$V_{\text{TFL}} = \frac{n_{\text{trap}} e L^2}{2 \epsilon_0 \epsilon_r}$$

where e is the unit charge (1.6×10^{-19} C), L is the thickness of PVK film ~ 600 nm, ϵ_0 is the vacuum permittivity (8.854×10^{-12} F/m), ϵ_r is the relative dielectric constant 28.8,

and n_{trap} is the trap state density. The V_{TFL} of the devices based on pristine PVK and passivated PVK is evaluated to be 0.41 V and 0.29 V, respectively. Therefore, the trap state density per cubic centimeter is declined from 3.63×10^{15} (the pristine PVK film) to 2.57×10^{15} (the passivated PVK film). This result indicates that the CuSCN passivation effectively improves the quality of the PVK film.

To analyze the internal and interfacial carrier dynamics of devices, linear sweep voltammetry (LSV), electrochemical impedance spectroscopy (EIS), transient photocurrent (TPC), steady-state photoluminescence (PL), and time-resolved photoluminescence (TRPL) spectra were measured. LSV results in Figure S8 and Figure 4a indicate that the interfacial conductivity of the passivated PVK/CuSCN layer is obviously higher than that of the pristine PVK/CuSCN layer, which implies the faster charge transport and less energy loss. EIS in Figure 4b display a similar series resistance (R_s), smaller transfer resistance (R_{tr}), and larger recombination resistance (R_{rec}) at the passivated PVK/CuSCN layer, where R_s , R_{tr} and R_{rec} correspond to the value of the starting point at the real part, the small arc in high frequency, and the large arc in low frequency. This indicates that the improved carrier transport and suppressed recombination are achieved at the passivated PVK/CuSCN layer interface. TPC measurements in Figure 4c show that the more efficient charge transfer occurs across the interface between passivated PVK and CuSCN layer. PL and TRPL spectra in Figure S9 and Figure 4d, measured by FTO/PVK (or passivated PVK)/CuSCN half-devices, show that stronger PL quenching and shorter carrier lifetime at the passivated PVK/CuSCN interface. That demonstrates the higher extraction and faster transfer of hole carriers. TRPL decays are fitted by using a biexponential decay equation, where τ_1 and τ_2 represent fast and slow decay time constant [42]. In this work, τ_2 is closely related to radiative recombination of free carriers across the PVK/CuSCN interface. In comparison with the pristine PVK/CuSCN interface ($\tau_2 = 31.08$ ns), shorter carrier lifetime ($\tau_2 = 24.01$ ns) of the passivated PVK/CuSCN interface demonstrates the accelerated extraction and transfer

of hole carriers.

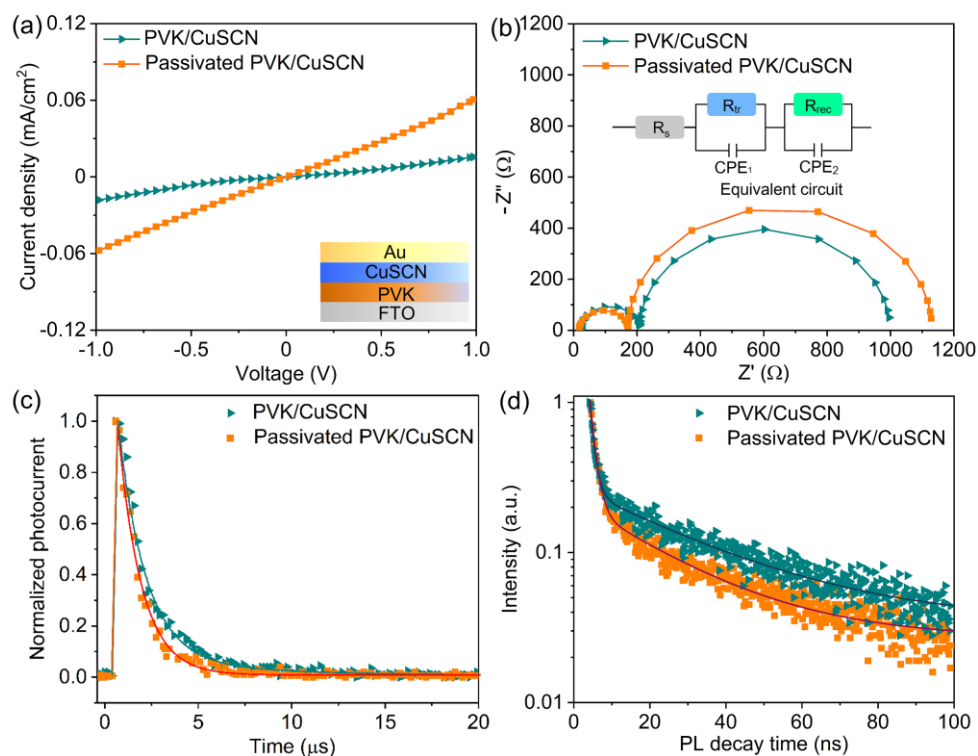


Figure 4. (a) LSV characteristics of FTO/PVK/CuSCN/Au and FTO/passivated PVK/CuSCN/Au structures, (b) EIS and (c) TPC decays of the whole devices with FTO/SnO₂/PVK/CuSCN/Carbon and FTO/SnO₂/passivated PVK/CuSCN/Carbon structures, (d) TRPL spectra of half-devices with FTO/PVK/CuSCN and FTO/passivated PVK/CuSCN structures.

To study the effect of the improved interfacial properties on the photovoltaic performance, C-PSCs based on the pristine PVK/CuSCN and the passivated PVK/CuSCN heterojunctions are fabricated. The cross-sectional SEM images are displayed in Figure S10 and Figure 5a. Comparing with the voids and defects at the pristine PVK/CuSCN layer interface, the interfacial contact between the passivated PVK and the CuSCN layer is almost smooth and seamless. Figure 5b shows the current density–voltage (J – V) characteristics of the champion C-PSCs based on the pristine PVK/CuSCN and the passivated PVK/CuSCN, measuring via reverse scan (RS) and forward scan (FS). The corresponding parameters are listed in Table 1. The optimal C-PSC based on the pristine PVK/CuSCN obtains a PCE of 13.59%, whereas

the champion C-PSC based on the passivated PVK/CuSCN yields a PCE of 15.81%. The hysteresis index (HI) of both C-PSCs is calculated by the previous method (Table S2) [43]. Although nonnegligible hysteresis exhibits in two types of C-PSCs, HI of the C-PSC based on the passivated PVK/CuSCN is smaller (0.105) than that of the C-PSC based on the pristine PVK/CuSCN (0.175). This is closely related to the improved interfacial carrier transfer and the decreased trap-state density. The incident photon-to-current conversion efficiency (IPCE) spectra in Figure 5c is in good agreement with the $J-V$ test results. To determine the operation stability of the C-PSCs, stabilized power output was recorded at their maximum power point (MPP) under full-sun illumination, as shown in Figure S11. After MPP tracking for 500 s, PCE of 12.60% and 14.98% are yielded for the devices based on the pristine PVK/CuSCN and the passivated PVK/CuSCN, respectively. Statistical PCE of 50 devices for two types of C-PSCs in Figure 5d indicates their good reproducibility, with the average PCE of C-PSCs based on the passivated PVK/CuSCN (14.09%) being $\sim 16.4\%$ higher than that of the C-PSCs based on the pristine PVK/CuSCN (12.11%).

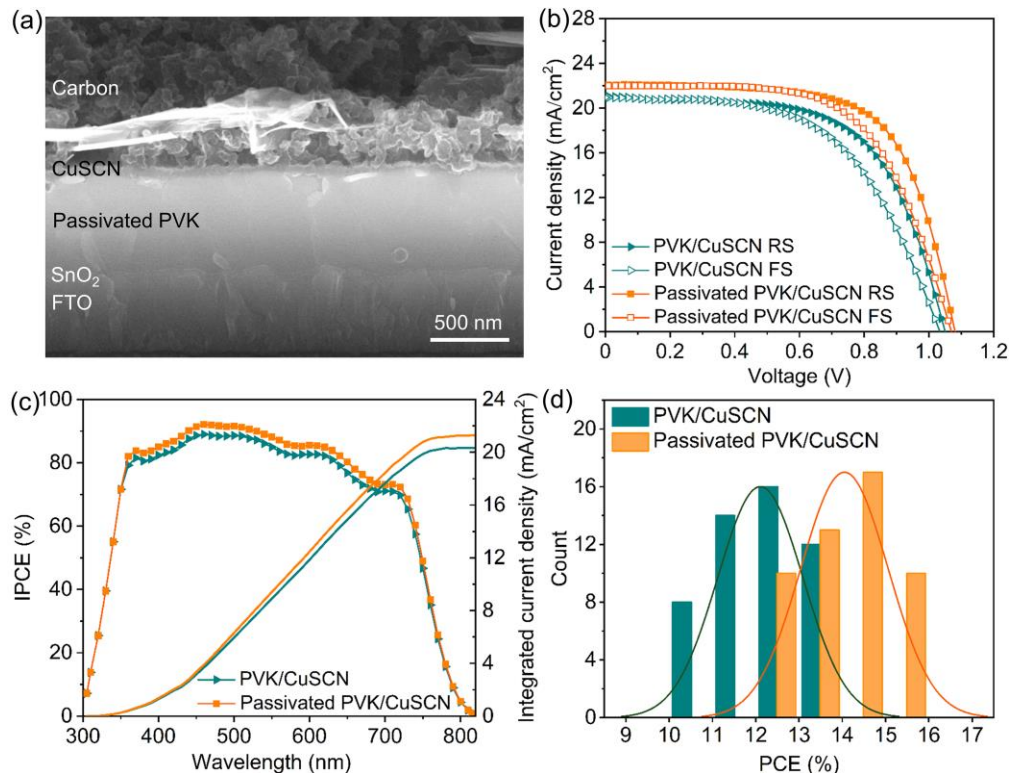


Figure 5. (a) The cross-sectional SEM image of the C-PSC with the passivated PVK/CuSCN, (b) $J-V$ curves of C-PSCs based on the pristine PVK/CuSCN and the passivated PVK/CuSCN via RS and FS, (c) IPCE spectra and the corresponding integrated current densities, (d) statistical PCE of 50 devices.

Table 1. Photovoltaic parameters of the champion C-PSCs based on the pristine PVK/CuSCN and the passivated PVK/CuSCN.

Device type	Scanning direction	V_{oc} (V)	J_{sc} (mA/cm ²)	FF (%)	PCE (%)
PVK/CuSCN	RS	1.049	21.07	61.5	13.59
	FS	1.029	20.94	56.2	12.11
Passivated PVK/CuSCN	RS	1.078	22.09	66.4	15.81
	FS	1.060	22.00	62.4	14.55

Notes: V_{oc} , open-circuit voltage; J_{sc} , short-circuit current density; FF, fill factor.

Long-term stability is one of the key parameters for PSCs. Both environmental and thermal stability of C-PSCs were evaluated. For environmental stability testing, the devices without any encapsulation were stored at ambient air with 22–32 °C and 30%–70% relative humidity (RH). After storage for 2000 h, C-PSCs based on the passivated PVK/CuSCN maintain ~93% of their initial PCE (Figure 6a), which is much higher than that of C-PSCs based on the pristine PVK/CuSCN (~67% of the initial PCE). For thermal stability testing, the encapsulated devices were continuously heated at 85 °C in dark ambient condition with <10% RH. The C-PSCs based on the passivated PVK/CuSCN and the pristine PVK/CuSCN could keep ~83% and ~57% of their initial PCE after aging for 300 h (Figure 6b). The C-PSCs based on the passivated PVK/CuSCN display the enhanced environmental and thermal stability. Two reasons give rise to this stability improvement. One is that the passivated PVK film shows enhanced hydrophobicity in comparison with the pristine PVK film, as shown in Figure S12. The other is the interfacial interaction between Pb^{2+} and SCN^- . The interaction between the PVK layer and the CuSCN hole transport layer was analyzed by XPS. A thin CuSCN layer (thickness: ~5 nm) was used as the hole

transport layer and deposited on the pristine PVK (or the passivated PVK) surface in order to detect the Pb 4f signals at the interfaces (Figure S13). As shown in Figure S14, the binding energy of Pb 4f at the pristine PVK/CuSCN interface and the passivated PVK/CuSCN interface shifts toward the lower binding energy, where the binding energy of Pb 4f shifts much more at the passivated PVK/CuSCN interface. This coupling effect could generate more reliable interfacial contact between the passivated PVK and the CuSCN hole transport layer, resulting in a robust interface to resist device degradation induced by environmental stress.

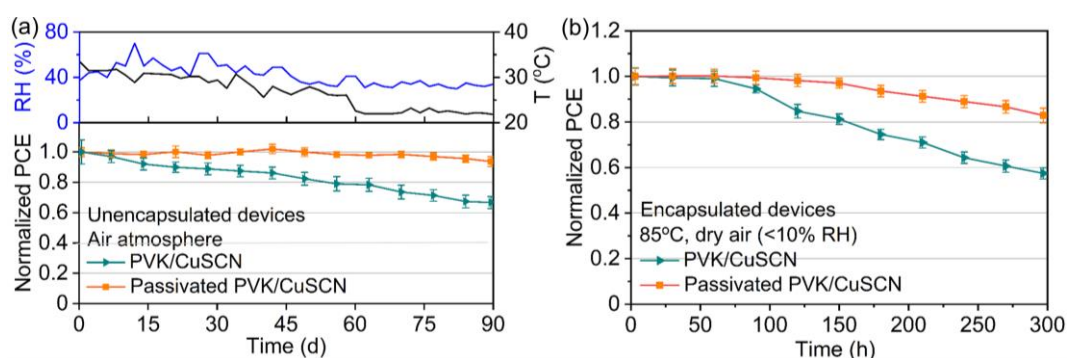


Figure 6. (a) Long-term stability of the C-PSCs without any encapsulation under monitored ambient air, including RH (blue curve, left axis) and temperature (black curve, right axis), and (b) thermal stability of the encapsulated C-PSCs in a dry air atmosphere (<10% RH) at constant 85 °C. Error bars with standard deviation display the PCE distribution of 10 cells from the same batch.

Conclusion

A new interfacial engineering designed on CuSCN is carried out for C-PSCs. It could improve the quality of PVK, passivate the trap states, enhance the interfacial connection, and give rise to accelerated charge extraction and transfer, which lead to an average PCE improvement by 16.4%. The optimal C-PSCs achieve a high PCE (15.81%) and good stability simultaneously. After storage for 2000 h at ambient air, devices without any encapsulation could maintain 93% of its initial efficiency. The stability improvement can be attributed to the enhanced hydrophobicity and the interfacial coupling effect of the passivated PVK film, which are favorable to resist

device degradation induced by environmental stress.

Acknowledgements

This work has received financial support from the National Natural Science Foundation of China (Grant No. 51772039, 21903010, and 51972293).

Conflicts of interest

None.

Reference

- [1] S.D. Stranks, G.E. Eperon, G. Grancini, C. Menelaou, M.J.P. Alcocer, T. Leijtens, L.M. Herz, A. Petrozza, H.J. Snaith, Electron-hole diffusion lengths exceeding 1 micrometer in an organometal trihalide perovskite absorber, *Science* 342 (2013) 341-344. <https://doi.org/10.1126/science.1243982>.
- [2] Y. Zhao, K. Zhu, Organic-inorganic hybrid lead halide perovskites for optoelectronic and electronic applications, *Chem. Soc. Rev.* 45 (2016) 655-689. <https://doi.org/10.1039/c4cs00458b>.
- [3] G. Xing, N. Mathews, S. Sun, S.S. Lim, Y.M. Lam, M. Graetzel, S. Mhaisalkar, T.C. Sum, Long-range balanced electron- and hole-transport lengths in organic-inorganic $\text{CH}_3\text{NH}_3\text{PbI}_3$, *Science* 342 (2013) 344-347. <https://doi.org/10.1126/science.1243167>.
- [4] S. Nair, S.B. Patel, J.V. Gohel, Recent trends in efficiency-stability improvement in perovskite solar cells, *Mater. Today Energy* 17 (2020) 100493. <https://doi.org/10.1016/j.mtener.2020.100449>.
- [5] <https://www.nrel.gov/pv/assets/pdfs/pv-efficiency-chart>
- [6] J.A. Christians, P.A. Miranda Herrera, P.V. Kamat, Transformation of the excited state and photovoltaic efficiency of $\text{CH}_3\text{NH}_3\text{PbI}_3$ perovskite upon controlled exposure to humidified air, *J. Am. Chem. Soc.* 137 (2015) 1530-1538. <https://doi.org/10.1021/ja511132a>.
- [7] N. Aristidou, I. Sanchez-Molina, T. Chotchuangchutchaval, M. Brown, L. Martinez, T. Rath, S.A. Haque, The role of oxygen in the degradation of methylammonium lead trihalide perovskite photoactive layers, *Angew. Chem. Int. Ed.* 54 (2015) 8208-8212. <https://doi.org/10.1002/anie.201503153>.
- [8] N. Aristidou, C. Eames, I. Sanchez-Molina, X. Bu, J. Kosco, M.S. Islam, S.A. Haque, Fast oxygen diffusion and iodide defects mediate oxygen-induced degradation of perovskite solar cells, *Nat. Commun.* 8 (2017) 15218. <https://doi.org/10.1038/ncomms15218>.
- [9] Z. Li, Y. Zhao, X. Wang, Y. Sun, Z. Zhao, Y. Li, H. Zhou, Q. Chen, Cost analysis of perovskite tandem photovoltaics, *Joule* 2 (2018) 1559-1572. <https://doi.org/10.1016/j.joule.2018.05.001>.
- [10] J. Bing, D.S. Lee, Y. Cho, J. Zheng, Y. Li, S. Tang, M. Zhang, S. Huang, A.W.Y. Ho-Baillie, Understanding how chlorine additive in a dynamic sequential process affects $\text{FA}_{0.3}\text{MA}_{0.7}\text{PbI}_3$ perovskite film growth for solar cell application, *Mater. Today Energy* 18 (2020) 100551. <https://doi.org/10.1016/j.mtener.2020.100551>.
- [11] G. Grancini, C. Roldan-Carmona, I. Zimmermann, E. Mosconi, X. Lee, D. Martineau, S. Narbey, F.

- Oswald, F. De Angelis, M. Graetzel, M.K. Nazeeruddin, One-year stable perovskite solar cells by 2D/3D interface engineering, *Nat. Commun.* 8 (2017) 15684. <https://doi.org/10.1038/ncomms15684>.
- [12] F. Meng, Y. Zhou, L. Gao, Y. Li, A. Liu, Y. Li, C. Zhang, M. Fan, G. Wei, T. Ma, Environmental risks and strategies for long-term stability of carbon-based perovskite solar cells, *Mater. Today Energy* 19 (2021) 100590. <https://doi.org/10.1016/j.mtener.2020.100590>.
- [13] F. Meng, A. Liu, L. Gao, J. Cao, Y. Yan, N. Wang, M. Fan, G. Wei, T. Ma, Current progress in interfacial engineering of carbon-based perovskite solar cells, *J. Mater. Chem. A* 7 (2019) 8690-8699. <https://doi.org/10.1039/c9ta01364d>.
- [14] H. Zhang, K. Song, L. Zhu, Q. Meng, Back-interface regulation for carbon-based perovskite solar cells, *Carbon* 168 (2020) 372-391. <https://doi.org/10.1016/j.carbon.2020.06.065>.
- [15] H. Chen, S. Yang, Methods and strategies for achieving high-performance carbon-based perovskite solar cells without hole transport materials, *J. Mater. Chem. A* 7 (2019) 15476-15490. <https://doi.org/10.1039/c9ta04707g>.
- [16] T. Malinauskas, D. Tomkute-Luksiene, R. Sens, M. Daskeviciene, R. Send, H. Wonneberger, V. Jankauskas, I. Bruder, V. Getautis, Enhancing thermal stability and lifetime of solid-state dye-sensitized solar cells via molecular engineering of the hole-transporting material Spiro-OMeTAD, *ACS Appl. Mater. Interfaces* 7 (2015) 11107-11116. <https://doi.org/10.1021/am5090385>.
- [17] S. Gholipour, J.-P. Correa-Baena, K. Domanski, T. Matsui, L. Steier, F. Giordano, F. Tajabadi, W. Tress, M. Saliba, A. Abate, A. Morteza Ali, N. Taghavinia, M. Grätzel, A. Hagfeldt, Highly efficient and stable perovskite solar cells based on a low-cost carbon cloth, *Adv. Energy Mater.* 6 (2016) 1601116. <https://doi.org/10.1002/aenm.201601116>.
- [18] S. Chae, A. Yi, H.J. Kim, Molecular engineering of a conjugated polymer as a hole transporting layer for versatile p-i-n perovskite solar cells, *Mater. Today Energy* 14 (2019) 100341. <https://doi.org/10.1016/j.mtener.2019.100341>.
- [19] Y. Yang, N.D. Pham, D. Yao, L. Fan, M.T. Hoang, V.T. Tiong, Z. Wang, H. Zhu, H. Wang, Interface engineering to eliminate hysteresis of carbon-based planar heterojunction perovskite solar cells via CuSCN incorporation, *ACS Appl. Mater. Interfaces* 11 (2019) 28431-28441. <https://doi.org/10.1021/acsami.9b07318>.
- [20] S. Liu, W. Huang, P. Liao, N. Pootrakulchote, H. Li, J. Lu, J. Li, F. Huang, X. Shai, X. Zhao, Y. Shen, Y.-B. Cheng, M. Wang, 17% efficient printable mesoscopic PIN metal oxide framework perovskite solar cells using cesium-containing triple cation perovskite, *J. Mater. Chem. A* 5 (2017) 22952-22958. <https://doi.org/10.1039/c7ta07660f>.
- [21] J.A. Christians, R.C. Fung, P.V. Kamat, An inorganic hole conductor for organo-lead halide perovskite solar cells. Improved hole conductivity with copper iodide, *J. Am. Chem. Soc.* 136 (2014) 758-764. <https://doi.org/10.1021/ja411014k>.
- [22] F. Zhang, X. Yang, M. Cheng, W. Wang, L. Sun, Boosting the efficiency and the stability of low cost perovskite solar cells by using CuPc nanorods as hole transport material and carbon as counter electrode, *Nano Energy* 20 (2016) 108-116. <https://doi.org/10.1016/j.nanoen.2015.11.034>.
- [23] R. Hu, R. Zhang, Y. Ma, W. Liu, L. Chu, W. Mao, J. Zhang, J. Yang, Y. Pu, X.a. Li, Enhanced hole transfer in hole-conductor-free perovskite solar cells via incorporating CuS into carbon electrodes, *Appl. Surf. Sci.* 462 (2018) 840-846. <https://doi.org/10.1016/j.apsusc.2018.08.078>.
- [24] J.E. Jaffe, T.C. Kaspar, T.C. Droubay, T. Varga, M.E. Bowden, G.J. Exarhos, Electronic and defect

- structures of CuSCN, *J. Phys. Chem. C* 114 (2010) 9111-9117. <https://doi.org/10.1021/jp101586g>.
- [25] S. Mashhoun, Y. Hou, H. Chen, F. Tajabadi, N. Taghavinia, H.-J. Egelhaaf, C.J. Brabec, Resolving a critical instability in perovskite solar cells by designing a scalable and printable carbon based electrode-interface architecture, *Adv. Energy Mater.* 8 (2018) 1802085. <https://doi.org/10.1002/aenm.201802085>.
- [26] X. Wu, L. Xie, K. Lin, J. Lu, K. Wang, W. Feng, B. Fan, P. Yin, Z. Wei, Efficient and stable carbon-based perovskite solar cells enabled by the inorganic interface of CuSCN and carbon nanotubes, *J. Mater. Chem. A* 7 (2019) 12236-12243. <https://doi.org/10.1039/c9ta02014d>.
- [27] N. Arora, M.I. Dar, S. Akin, R. Uchida, T. Baumeler, Y. Liu, S.M. Zakeeruddin, M. Gratzel, Low-cost and highly efficient carbon-based perovskite solar cells exhibiting excellent long-term operational and UV stability, *Small* 15 (2019) 1904746. <https://doi.org/10.1002/sml.201904746>.
- [28] Y. Yang, M.T. Hoang, D. Yao, P. Duy Ngoc, V.T. Tiong, X. Wang, H. Wang, Spiro-OMeTAD or CuSCN as a preferable hole transport material for carbon-based planar perovskite solar cells, *J. Mater. Chem. A* 8 (2020) 12723-12734. <https://doi.org/10.1039/d0ta03951a>.
- [29] I. Zimmermann, P. Gratia, D. Martineau, G. Grancini, J.-N. Audinot, T. Wirtz, M.K. Nazeeruddin, Improved efficiency and reduced hysteresis in ultra-stable fully printable mesoscopic perovskite solar cells through incorporation of CuSCN into the perovskite layer, *J. Mater. Chem. A* 7 (2019) 8073-8077. <https://doi.org/10.1039/c9ta00669a>.
- [30] P. Worakajit, F. Hamada, D. Sahu, P. Kidkhunthod, T. Sudyoadsuk, V. Promarak, D.J. Harding, D.M. Packwood, A. Saeki, P. Pattanasattayavong, Elucidating the coordination of diethyl sulfide molecules in Copper(I) Thiocyanate (CuSCN) thin films and improving hole transport by antisolvent treatment, *Adv. Funct. Mater.* 30 (2020) 2002355. <https://doi.org/10.1002/adfm.202002355>.
- [31] M. Samadpour, A. Golchini, K. Abdizadeh, M. Heydari, M. Forouzandeh, Z. Saki, N. Taghavinia, Modified antisolvent method for improving the performance and stability of triple-cation perovskite solar cells, *ACS Omega* 6 (2021) 172-179. <https://doi.org/10.1021/acsomega.0c04058>.
- [32] M. Wang, Q. Fu, L. Yan, P. Guo, L. Zhou, G. Wang, Z. Zheng, W. Luo, Improving the performance and reproducibility of inverted planar perovskite solar cells using tetraethyl orthosilicate as the antisolvent, *ACS Appl. Mater. Interfaces* 11 (2019) 3909-3916. <https://doi.org/10.1021/acsomega.8b18402>.
- [33] D. Prochowicz, M.M. Tavakoli, A. Solanki, T.W. Goh, K. Pandey, T.C. Sum, M. Saliba, P. Yadav, Understanding the effect of chlorobenzene and isopropanol anti-solvent treatments on the recombination and interfacial charge accumulation in efficient planar perovskite solar cells, *J. Mater. Chem. A* 6 (2018) 14307-14314. <https://doi.org/10.1039/c8ta03782e>.
- [34] S. Paek, P. Schouwink, E.N. Athanasopoulou, K.T. Cho, G. Grancini, Y. Lee, Y. Zhang, F. Stellacci, M.K. Nazeeruddin, P. Gao, From Nano- to Micrometer Scale: The role of antisolvent treatment on high performance perovskite solar cells, *Chem. Mater.* 29 (2017) 3490-3498. <https://doi.org/10.1021/acs.chemmater.6b05353>.
- [35] S. Ye, H. Rao, W. Yan, Y. Li, W. Sun, H. Peng, Z. Liu, Z. Bian, Y. Li, C. Huang, A strategy to simplify the preparation process of perovskite solar cells by co-deposition of a hole-conductor and a perovskite layer, *Adv. Mater.* 28 (2016) 9648-9654. <https://doi.org/10.1002/adma.201603850>.
- [36] Z. Guo, L. Gao, Z. Xu, S. Teo, C. Zhang, Y. Kamata, S. Hayase, T. Ma, High electrical conductivity 2D MXene serves as additive of perovskite for efficient solar cells, *Small* 14 (2018)

1802738. <https://doi.org/10.1002/sml.201802738>.

[37] M. Hadadian, J.-P. Correa-Baena, E.K. Goharshadi, A. Ummadisingu, J.-Y. Seo, J. Luo, S. Gholipour, S.M. Zakeeruddin, M. Saliba, A. Abate, M. Gratzel, A. Hagfeldt, Enhancing efficiency of perovskite solar cells via N-doped Graphene: Crystal modification and surface passivation, *Adv. Mater.* 28 (2016) 8681-8686. <https://doi.org/10.1002/adma.201602785>.

[38] H. Yi, L. Duan, F. Haque, J. Bing, J. Zheng, Y. Yang, A.C.-h. Mo, Y. Zhang, C. Xu, G. Conibeer, A. Uddin, Thiocyanate assisted nucleation for high performance mix-cation perovskite solar cells with improved stability, *J. Power Sources* 466 (2020) 228320. <https://doi.org/10.1016/j.jpowsour.2020.228320>.

[39] J. Ge, W. Li, X. He, H. Chen, W. Fang, X. Du, Y. Li, L. Zhao, Charge behavior modulation by titanium-carbide quantum dots and nanosheets for efficient perovskite solar cells, *Mater. Today Energy* 18 (2020) 100562. <https://doi.org/10.1016/j.mtener.2020.100562>.

[40] D. Bi, C. Yi, J. Luo, J.-D. Décoppet, F. Zhang, Shaik M. Zakeeruddin, X. Li, A. Hagfeldt, M. Grätzel, Polymer-templated nucleation and crystal growth of perovskite films for solar cells with efficiency greater than 21%, *Nat. Energy* 1 (2016) 16142. <https://doi.org/10.1038/nenergy.2016.142>.

[41] X. Shi, Y. Wu, J. Chen, M. Cai, Y. Yang, X. Liu, Y. Tao, M. Guli, Y. Ding, S. Dai, Thermally stable perovskite solar cells with efficiency over 21% via a bifunctional additive, *J. Mater. Chem. A* 8 (2020) 7205-7213. <https://doi.org/10.1039/d0ta01255f>.

[42] C. Liu, L. Zhang, Y. Li, X. Zhou, S. She, X. Wang, Y. Tian, A.K.Y. Jen, B. Xu, Highly stable and efficient perovskite solar cells with 22.0% efficiency based on inorganic-organic dopant-free double hole transporting layers, *Adv. Funct. Mater.* 30 (2020) 1908462. <https://doi.org/10.1002/adfm.201908462>.

[43] F. Meng, L. Gao, Y. Yan, J. Cao, N. Wang, T. Wang, T. Ma, Ultra-low-cost coal-based carbon electrodes with seamless interfacial contact for effective sandwich-structured perovskite solar cells, *Carbon* 145 (2019) 290-296. <https://doi.org/10.1016/j.carbon.2019.01.047>.